

LARGE EDDY SIMULATION OF THE FLOW OVER A CONTOURED RAMP

Christer Fureby

Defence Security Systems Technology
The Swedish Defence Research Agency (FOI)
SE 147 25 Tumba, Stockholm, Sweden
fureby@foi.se

Shuang Zhu

Maritime Platforms Division
Defence Science and Technology Organisation (DSTO),
506 Lorimer St., Fishermans Bend, Victoria 3207, Melbourne Australia
Shuang.Zhu@dsto.defence.gov.au

David Jones

Maritime Platforms Division
Defence Science and Technology Organisation (DSTO),
506 Lorimer St., Fishermans Bend, Victoria 3207, Melbourne Australia
David.Jones@dsto.defence.gov.au

ABSTRACT

Large Eddy Simulations (LES) have been used to simulate the development, separation, reattachment and downstream recovery of the flow over a smoothly contoured ramp. Five different subgrid models have been compared on a grid of intermediate resolution containing 19.2 million cells and the effect of grid resolution has been examined by studying the behavior of one model on four different grids varying between 2.4 and 153.6 million cells. All LES models capture the main flow features, but the results on the intermediate and fine grids generally show better agreement with the experimental data.

INTRODUCTION

External flows around ships, submarines, cars, trains and airplanes and internal flows in e.g. turbomachinery are often complicated and fully three-dimensional (3D) and contain curved surfaces, pressure gradients, rotation effects and other complicated non-equilibrium effects. In these situations equilibrium turbulent boundary layers may no longer exist, and the boundary layer properties become obfuscated, and separation may occur in the presence of a pressure gradient. The understanding and predictive capabilities of non-equilibrium boundary layers are less well understood compared with that of equilibrium flows. The study of boundary layer separation, reattachment and downstream recovery is important as they influence the performance of many engineering applications such as the ones mentioned. Reynolds Averaged Navier-Stokes (RANS) simulations typically provide meager predictions of separated flow while Large Eddy Simulation (LES) is showing an improved capability in this regard.

The aim of this paper therefore is to improve our cur-

rent understanding of high Reynolds (Re) turbulent separating flow around curved geometries using LES. More specifically we consider the flow over the contoured ramp of Song *et al.* (2000) and Song & Eaton (2004), which is a well-defined flow exhibiting a small and shallow but distinct separation bubble far downstream on the ramp. Experimental surface pressures along the ramp and velocity profiles across the channel at different locations are available for comparison. We use an in-house LES code developed within the framework of OpenFOAM, Weller *et al.* (1996). This code includes most modern subgrid models and here we focus on the use of the Wall Adaptive Localized Eddy (WALE) viscosity model of Nicoud & Ducros (1999), the Mixed Model (MM) of Bardina *et al.* (1980) and Bensow & Fureby (2008), the Localized Dynamic k-Equation Model (LDKM) of Kim & Menon (1999), the One Equation Eddy Viscosity Model (OEEVM) of Yoshizawa & Horiuti (1985), and an Implicit LES formulation (ILES), Fureby & Grinstein (2002). We compare the accuracy of these different models on a grid of intermediate resolution containing 19.2 million cells as well as the effect of mesh resolution on the simulated results by studying the LDKM model on four different grids varying between 2.4 million and 153.6 million cells.

THE CONTOURED RAMP

The contoured ramp experiments against which the simulations will be compared were carried out in a closed-loop wind tunnel, DeGraaf & Eaton (1999), with a rectilinear test section of $0.152 \times 0.711 \times 3.000 \text{ m}^3$. For this experiment a special insert was placed into the rectangular test section to form the ramp geometry. The physical domain is then a flat plate followed by a smoothly contoured ramp and an-

other flat plate region. The upstream approach channel is 2.000 m long and the radius of curvature of the ramp is $R=0.127$ m, while its length and height are $L_r=0.070$ m and $h=0.021$ m, respectively. The channel section following the ramp has a length of 0.700 m. An upper wall is present 0.131 m above the floor of the ramp, far enough that the two boundary layers are separated by a core flow whose height is equal to about three boundary layer thicknesses at the inlet of the computational domain. The experimental study is summarized by Song *et al.* (2000) and Song & Eaton (2004), and consists of time-averaged and rms velocity profiles from customized Laser Doppler Anemometry (LDA) measurements at numerous cross sections upstream of, along, and downstream of the contoured ramp, as well as wall-pressure data

Simulations of this flow have previously been reported by Wasistho & Squires (2001), using 2D RANS based on the Spalart & Allmaras (1994) and Durbin (1991) v^2 -f models, and LES, using 2.93 million cells using the dynamic Smagorinsky model (Germano *et al.*, 1991) and a precursor boundary layer simulation to account for the gradually developing turbulent flow along the lower wind tunnel wall. Radhakrishnan *et al.* (2006) studied this flow using DES, using 1.58 and 5.70 million cells, based on the Spalart-Allmaras model (Nikitin *et al.*, 1999) and stochastic forcing of the RANS-LES transition region, together with a pre-cursor boundary layer simulation similar to that utilized by Wasistho & Squires (2001). El-Askary (2009) computed this flow using Implicit LES, using 1.74 million cells, again together with a pre-cursor boundary layer simulation similar to that of Wasistho & Squires (2001).

The results are generally reasonably good when compared with the experimental data, but all simulations share the use of pre-cursor boundary layer simulations to handle the gradually developing turbulent flow along the lower wind tunnel wall and a relatively narrow spanwise width together with periodic boundary conditions. The range of grids examined is also rather narrow.

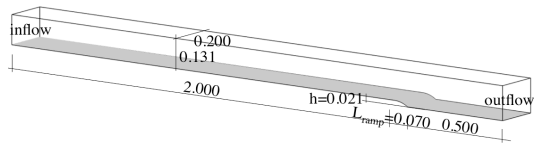


Figure 1. Schematic of the computational domain used in this study.

In the LES reported here the computational domain has been extended to account for the entire upstream approach channel, at the beginning of which a fixed velocity profile together with a zero Neumann condition for the pressure is applied. At the outflow a Dirichlet condition is used for pressure together with a zero Neumann condition for the velocity. No-slip conditions are applied on the top and bottom walls and slip conditions are used on the lateral sides of the computational configuration being 0.200 m apart. For this comparison four topologically similar grids have been generated with 2.4 Mcells (very coarse), 8.1 Mcells (coarse), 19.2 Mcells (intermediate) and 153.6 Mcells (fine), respectively. Based on the inflow velocity,

$v_0=20.4$ m/s, and the step height of the ramp the integral Re number of this flow is 28,560, which together with the complex, partially or intermittently separating and reattaching, flow makes this case challenging. Figure 1 shows a schematic of the computational configuration.

LARGE EDDY SIMULATION (LES) MODELING

LES is based on a separation of scales using spatial filtering, Sagaut (2001). Flow physics on scales larger than the filter width, Δ , are resolved, whereas flow physics on scales below Δ are modeled using a subgrid model. For a linear viscous incompressible fluid, the LES equations are,

$$\partial_t(\bar{\mathbf{v}})+\nabla\cdot(\bar{\mathbf{v}}\otimes\bar{\mathbf{v}})=-\nabla\bar{p}+\nabla\cdot(\bar{\mathbf{S}}-\mathbf{B}), \quad \nabla\cdot\bar{\mathbf{v}}=0, \quad (1)$$

where \mathbf{v} is the velocity, p the pressure, $\mathbf{S}=2\nu\mathbf{D}_D$ the viscous stress tensor, ν the viscosity and $\mathbf{D}_D=\frac{1}{2}(\nabla\mathbf{v}+\nabla\mathbf{v}^T)$ the rate-of-strain tensor and $\mathbf{B}=(\mathbf{v}\otimes\mathbf{v}-\bar{\mathbf{v}}\otimes\bar{\mathbf{v}})$ the subgrid stress tensor, representing the effects of the unresolved transport of momentum on the resolved flow. Here, and in what follows, overbars indicates filtered variables.

In order to close (1) and to represent the physics of the unresolved flow, \mathbf{B} must be modeled. By manipulating the raw and filtered momentum equations a transport equation for \mathbf{B} can be formulated. This equation is of the form,

$$\partial_t(\mathbf{B})+\nabla\cdot(\mathbf{B}\otimes\bar{\mathbf{v}})=-\mathbf{P}(\mathbf{B}\bar{\mathbf{v}}+\nabla\bar{\mathbf{v}}^T\mathbf{B})-\nabla\mathbf{J}+\Phi-\mathbf{E}, \quad (2)$$

in which $\mathbf{P}=\mathbf{B}\bar{\mathbf{v}}+\nabla\bar{\mathbf{v}}^T\mathbf{B}$ is the exact production term, \mathbf{J} the redistribution tensor, Φ the subgrid pressure strain correlation, and \mathbf{E} the subgrid destruction term. An mathematical solution to (2) was recently offered by Li *et al.* (2009) in terms of matrix exponentials, such that,

$$\mathbf{B}=\frac{2}{3}k\mathbf{I}-\nu_k\bar{\mathbf{D}}_D+\nu\tau_k(\bar{\mathbf{D}}_D^2+\frac{1}{2}(\bar{\mathbf{W}}\bar{\mathbf{D}}-\bar{\mathbf{D}}\bar{\mathbf{W}}))+\dots, \quad (3)$$

in which $\mathbf{W}=\frac{1}{2}(\nabla\mathbf{v}-\nabla\mathbf{v}^T)$, ν_k a subgrid viscosity and τ_k a subgrid time scale. Following Bensow & Fureby (2008), the intrinsic nature of \mathbf{B} encourages a decomposition into Leonard, cross and Reynolds tensors,

$$\mathbf{B}=(\bar{\mathbf{v}}\otimes\bar{\mathbf{v}}-\bar{\bar{\mathbf{v}}}\otimes\bar{\bar{\mathbf{v}}})+(\bar{\mathbf{v}}\otimes\bar{\mathbf{v}}'-\bar{\bar{\mathbf{v}}}\otimes\bar{\mathbf{v}}'+\bar{\mathbf{v}}'\otimes\bar{\mathbf{v}}-\bar{\bar{\mathbf{v}}}'\otimes\bar{\bar{\mathbf{v}}}')+(\bar{\mathbf{v}}'\otimes\bar{\mathbf{v}}'-\bar{\mathbf{v}}'\otimes\bar{\mathbf{v}}'), \quad (4)$$

of which the Leonard tensor $\mathbf{L}=(\bar{\mathbf{v}}\otimes\bar{\mathbf{v}}-\bar{\bar{\mathbf{v}}}\otimes\bar{\bar{\mathbf{v}}})$ can be explicitly computed, thus reducing the need for modeling to the sum of the cross and Reynolds tensors.

Here, five different closure models will be examined: Three of these models are based on the linear terms in (3) corresponding to the Boussinesq approximation. The first of these is the Wall Adapting Local Eddy Viscosity Model (WALE) of Nicoud & Ducros (1999) in which,

$$\mathbf{B}=-2\nu_k\bar{\mathbf{D}}_D=-c_w^2\Delta^2\left(\frac{(\bar{\mathbf{G}}_D\bar{\mathbf{G}}_D)^2}{(\bar{\mathbf{D}}\bar{\mathbf{D}})^{3/2}+(\bar{\mathbf{G}}_D\bar{\mathbf{G}}_D)^{3/4}}\right)\bar{\mathbf{D}}_D, \quad (5)$$

where $c_w=0.325$. The second of these is the One Equation Eddy Viscosity Model (OEEVM), of Yoshizawa & Horiuti (1985) which is based on a k equation,

$$\mathbf{B}=-2\nu_k\bar{\mathbf{D}}_D=-2c_k\Delta k^{1/2}\bar{\mathbf{D}}_D,$$

$$\partial_t(k)+\nabla(k\bar{v})=c_k\Delta k^{1/2}|\bar{\mathbf{D}}|^2+\nabla(v_k\nabla k)-c_\epsilon k^{3/2}/\Delta, \quad (6)$$

where $c_k=0.07$ and $c_\epsilon=1.03$ as evaluated from an inertial range spectra. The third model of this class is the Localized Dynamic k-Equation Model (LDKM) of Kim & Menon (1999) which is also based on (6) but with model coefficients computed dynamically using scale-similarity,

$$c_k=-\frac{(\mathbf{L}\mathbf{M})}{(2\mathbf{M}\mathbf{M})}, \quad c_\epsilon=2v_{\text{eff}}\Delta((\nabla\bar{v})^2-(\bar{\nabla v})^2)/K^{3/2}, \quad (7)$$

in which $2K=\text{tr}(\mathbf{L})$ and $\mathbf{M}=\bar{\Delta}K^{1/2}\bar{\mathbf{D}}$. The fourth model examined is the Mixed Model (MM) of Bardina *et al.* (1980) and Bensow & Fureby (2008) based on (4) in which,

$$\mathbf{B}=(\bar{v}\otimes\bar{v}-\bar{v}\otimes\bar{v})-2c_k\Delta k^{1/2}\bar{\mathbf{D}}, \quad (8)$$

in which k is obtained from the OEEVM (6). The fifth and last model examined in an Implicit LES (ILES) model of Fureby & Grinstein (2002), in which the raw (or unfiltered) Navier-Stokes equations are solved using monotonicity preserving flux reconstruction algorithms that can be shown (Fureby & Grinstein, 2002), to result in a leading order truncation error of the form,

$$\mathbf{B}=\mathbf{C}(\nabla\mathbf{v})^T+(\nabla\mathbf{v})\mathbf{C}^T+\chi^2(\nabla\mathbf{v})\mathbf{d}\otimes(\nabla\mathbf{v})\mathbf{d}+\dots, \quad (9)$$

formally resembling the matrix exponential solution (3) to the transport equation (2), in which $\mathbf{C}=\chi(\mathbf{v}\otimes\mathbf{d})$ with χ being a non-linear function of the flux limiter Ψ .

The code used is OpenFOAM, Weller *et al.* (1996), in which the discretization is based on unstructured finite volumes. For all LES models the discretization uses linear reconstruction of the convective fluxes and central differencing of the viscous flux terms with compact 2nd order stencils and time integration is performed by explicit 2nd order backward differencing which guarantees overall 2nd order accuracy and low numerical diffusion. For ILES the convective fluxes are reconstructed using the monotonicity preserving Gamma algorithm of Jasak (1996) based on the blending of a linear and an upwind biased scheme using a non-linear flux limiter. The pressure-velocity coupling is handled with the PISO algorithm, and the equations are solved sequentially with $\text{CFL}<0.3$.

RESULTS

Figure 2 shows the resulting flow in terms of iso-surfaces of the second invariant of the velocity gradient tensor, λ_2 , the instantaneous streamwise velocity, v_x , and the friction velocity, u_τ , at the lower wall from the LES-WALE model on the intermediate grid. The LES-WALE result is representative of the different LES models investigated on the intermediate and fine grids, whereas fewer vortical structures are observed in the boundary layers on the coarse grid. Downstream of the inflow the initial velocity profile gradually transitions into a turbulent velocity profile as the boundary layer develops. The transition length is different for different subgrid models and is strongly dependent on the grid resolution but with the intermediate and fine grids showing similar transition behaviors. Further downstream, the boundary layer continues to develop and progressively

thickens towards the ramp section. At the ramp, a shallow recirculation region is observed for all LES, with the separation and reattachment locations differing for each model. Not surprisingly, these locations approach those of the experiments with increasing grid resolution irrespective of the subgrid model.

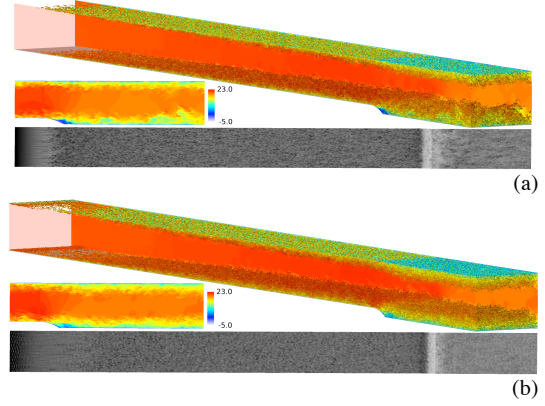


Figure 2. The flow in the computational domain in terms of the instantaneous velocity, v_x , iso-surfaces of the second invariant of the velocity gradient tensor, λ_2 , colored by v_x , and the friction velocity, u_τ , at the bottom wall from (a) the LES-WALE model and (b) the LES-MM model on the intermediate grid.

Figure 3 presents a magnified view of the downstream ramp section. The large-eddy structure near the wall in the approach boundary layers are adapted in several ways: by the mean shear, the blocking of the wall-normal velocity component and by the internal shear layers produced by large eddies as they impinge and scrape along the walls. Elongated axial vortices are formed with length scales that are several times the boundary layer height. The lower boundary layer separates approximately between $x/L_R \approx 0.50$ and 0.60 and reattaches around $x/L_R \approx 1.40$. The recirculation bubble fluctuates significantly in time, and along the spanwise direction, and is dynamically driven by the back-flow. Downstream, the flow recovers quickly to a virtually fully developed turbulent channel or boundary layer flow. The boundary and shear layer vortical structures coalesce to form clusters of vortical structures that continues to agglomerate into large scale axial and Ω -shaped flow structures that dominate further downstream whilst continuing to increase in size and entrainment strength.

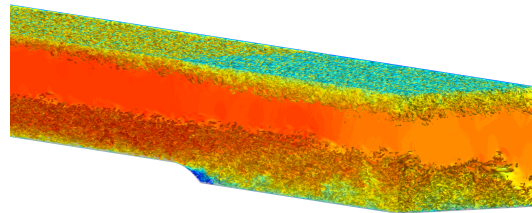


Figure 3. Iso-surfaces of the second invariant of the velocity gradient tensor, λ_2 , colored by the axial velocity, v_x , downstream of the contoured ramp from the LES-WALE model on the intermediate grid.

Figure 4 compares the time-averaged pressure coefficient, $c_p = (\langle p \rangle - p_0) / \frac{1}{2} \rho v_0^2$, in which p_0 is the freestream pressure, on the bottom wall between the experimental data and the different LES model predictions and for the different grids using the LES-LDKM model. On the lower wall, there is a favorable pressure gradient approaching the ramp up to $x/L_R \approx 0.20$ due to the wall curvature effect. After that, the flow expansion dominates, causing an adverse pressure gradient over the remainder of the ramp. There is a short plateau around the trailing edge of the ramp, $x/L_R \approx 1.00$. This indicates the presence of a separation bubble over the trailing edge as seen in figures 2 and 3. The dividing streamline of the separation bubble acts like a flat wall over a short length around the trailing edge. The adverse pressure gradient extends to $x/L_R \approx 2.00$. The boundary layer displacement thickness drops after the trailing edge of the ramp, resulting in a mild favorable pressure gradient at $x/L_R \approx 2.00$, after which it relaxes back to approximately zero pressure gradient. The results of the static pressure on the top wall (not shown) reveal that there is no separation on the top wall and show the static pressure increases monotonically over the ramp.

The grid resolution is found to influence the wall pressure distribution so that: on the coarse grid modest agreement with the experimental data is observed, but with increased grid resolution the agreement rapidly improves. On the intermediate grid all LES models capture the favorable pressure gradient approaching the ramp but underestimate the (negative) pressure at the beginning of the ramp. Similarly, all LES models capture the strong adverse pressure gradient over the rest of the ramp, but with notably different predictions of the short plateau around the trailing edge of the ramp, corresponding to the separation bubble. Best agreement is obtained with the WALE and LDKM models, whereas the MM noticeably overpredicts the pressure around the reattachment line, suggesting a too small separation bubble.

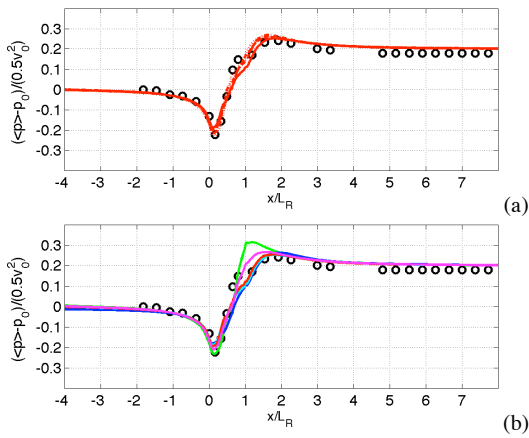


Figure 4. Time-averaged pressure coefficient for (a) different grids and (b) for different models on the intermediate grid. Legend: (○) experiments, (—) LES-WALE, (—) LES-MM, (—) LES-OEEVM, (—) LES-LDKM and (—) LES-ILES, (· · ·) very coarse grid, (---) coarse grid, (—) intermediate grid and (—) fine grid.

Figures 5a and 5b compares the time-averaged axial velocity, $\langle v_x \rangle / v_0$, in the equilibrium region ($x/L_R = -2.00$), at the start of the ramp ($x/L_R = 0.00$), near the mean separation ($x/L_R = 0.77$), in the separation bubble ($x/L_R = 1.00$), and in the recovery region ($x/L_R = 4.00$), between the experimental data and the different LES model predictions and for the different grids using the LES-LDKM model. In figures 5a and 5b, the profiles are positioned at the values of x/L_R to emphasize the relative shape of the time-averaged streamwise velocity compared to the shape of the wind tunnel and ramp. The ramp results in a favorable pressure gradient up to $x/L_R \approx 0.20$, causing the boundary layer to thin. Once in the adverse pressure gradient, the boundary layer thickness grows rapidly and the profiles develop an inflection point. In the experiments of Song & Eaton (2004) the boundary layer separates at $x/L_R \approx 0.77$ and reattaches at $x/L_R \approx 1.40$, whereas in all LES separation occurs slightly earlier, around $x/L_R \approx 0.50$ to 0.55 , but with reattachment taking place between $x/L_R \approx 1.30$ and 1.40 . The length of the separation bubble is therefore predicted to be slightly longer than what the experiments suggest.

The height of the separation bubble, which is defined to be where the mean velocity is equal to zero, is approximately $L_R/10$ at the trailing edge. The backflow in the separation bubble is clearly visible at the trailing edge. The recovery of the time-averaged flow is rather fast downstream of reattachment. By $x/L_R \approx 2.00$, the time-averaged flow profile has filled out considerably, although it still shows a considerable deficit in the outer layer. The time-averaged flow profiles at $x/L_R \approx 4.00$ and 7.00 , however, have essentially recovered almost to a fully developed flat plate boundary layer.

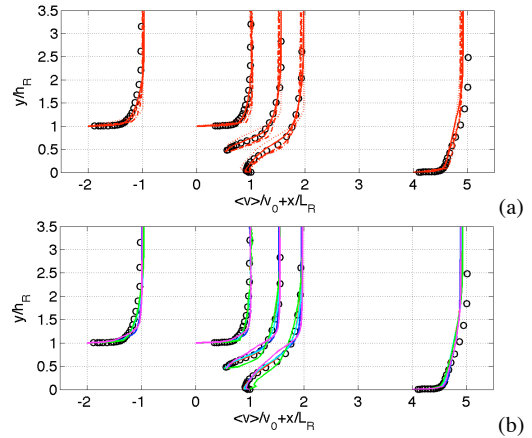


Figure 5. Time-averaged streamwise velocity for (a) different grids and (b) for different models on the intermediate grid. Legend: (○) experiments, (—) LES-WALE, (—) LES-MM, (—) LES-OEEVM (—) LES-LDKM and (—) LES-ILES, (· · ·) very coarse grid, (---) coarse grid, (—) intermediate grid and (—) fine grid.

All LES models capture the main flow features, but the results on the intermediate and fine grids generally show better agreement with the experimental data. The approach boundary layer and separation region are particularly better predicted on the intermediate and fine grids

than on the very coarse, and coarse grids. Regarding the predictive capabilities of the different LES models we find that the very coarse grid appears too coarse to predict the mean flow accurately. On the coarse grid the LDKM model shows the best overall agreement with the experimental data, whereas on the intermediate and fine grids the LDKM, WALE and ILES models all show virtually identical results in good agreement with the experimental data. Moreover, the MM model show better predictions on the coarse grid than on the intermediate and fine grid which is unexpected and not yet fully understood.

Figures 6a and 6b compare the axial rms-velocity fluctuations, v_x^{rms}/v_0 , in which $v_x^{\text{rms}} = \sqrt{\langle (v_x - \langle v_x \rangle)^2 \rangle}$ is the axial rms-velocity fluctuations, in the equilibrium region ($x/L_R = -2.00$), at the start of the ramp ($x/L_R = 0.00$), near separation ($x/L_R = 0.77$), in the separation bubble ($x/L_R = 1.00$), and in the recovery region ($x/L_R = 4.00$), between the experimental data and the different LES model predictions, and for the different grids using the LDKM model. Before the ramp, the axial rms-velocity peaks close to the inflection point of the time-averaged velocity profiles. In the adverse pressure gradient region, the axial rms-velocity profiles is significantly modified, with considerably wider profiles and peak levels about 50% higher than upstream of the ramp. Moreover, the peaks shift outwards moving downstream remaining in alignment with the inflection point in the time-averaged profile. The effects of the time-averaged profile distortion by the adverse pressure gradient appear to overwhelm the effects of the convex curvature upstream of separation. One might expect that the strong curvature would cause rapid suppression of the turbulence in the outer layer, but these results show that the outer layer axial rms-velocity increase when approaching separation. At $x/L_R = 4.00$ and 7.00 (not shown) the axial rms-velocity is essentially recovered near the wall, and the outer layer peak has decayed to form a plateau of constant normal stress, whereas further downstream the original profile gradually becomes reestablished.

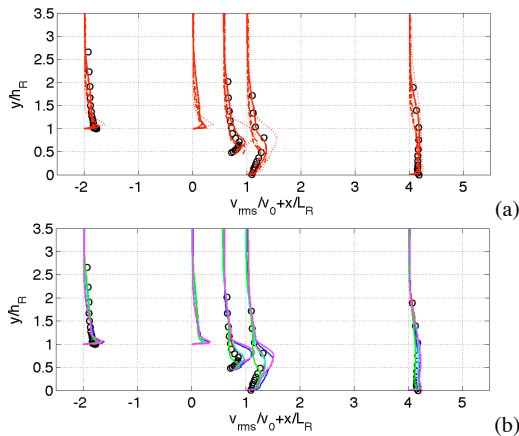


Figure 6. Axial rms-velocity fluctuations for (a) different grids and (b) for different models on the intermediate grid. Legend: (○) experiments, (—) LES-WALE, (—) LES-MM, (—) LES-OEEVM, (—) LES-LDKM and (—) LES-ILES, (•••) very coarse grid, (—•) coarse grid, (—) intermediate grid and (—) fine grid.

All LES models capture the turbulence, but the results on the intermediate and fine grids agree better with the experimental data. The turbulence in the approach boundary layer and in the separation region are better predicted on the intermediate and fine grids than on the very coarse and coarse grids, where it is usually overpredicted. Regarding the predictive capabilities of the LES models we find that the very coarse grid is too coarse to predict the mean flow. On the coarse grid the LDKM model shows the best overall agreement with the experimental data, whereas on the intermediate and fine grids the LDKM, ILES and WALE models all show very similar results, being in good agreement with the experimental data. Moreover, the MM model show better predictions on the coarse grid than on the intermediate and fine grid which is unexpected and not yet fully understood.

Figure 7 shows different aspects of the boundary layer flow: The upper figure shows the skin friction distribution together with the mean separation and reattachment lines from the WALE model on the intermediate grid, whereas the lower figure shows a combination of surface streamlines in black, vortex lines in dark red and contours of the first invariant of the no-slip tensor, Chong *et al.* (2012). The approach flow reveals the classical streaky structure of a developed flat plate turbulent boundary layer. The WALE, LDKM, ILES models all reveal separation at approximately $x/L_R \approx 0.50$ and reattachment at about $x/L_R \approx 1.40$ which is in agreement with the experimental data of Song & Eaton (2004) whereas the OEEVM and in particular the MM shows somewhat later separation. In particular the MM model shows a more shallow separation than the other LES models. Following Chong *et al.* (2012) we note that where the first invariant of the no-slip tensor, P , is zero, the flow is two-dimensional. It can be that although most of the surface flow is two-dimensional, the flow is 3D in regions near critical points, in regions where there are kinks in the vortex lines and close to separation and reattachment. Close to the three-dimensional regions apparent turbulent structures will instigate flow reversals close to the wall. This is most apparent, as expected, in the region between the separation and reattachment lines.

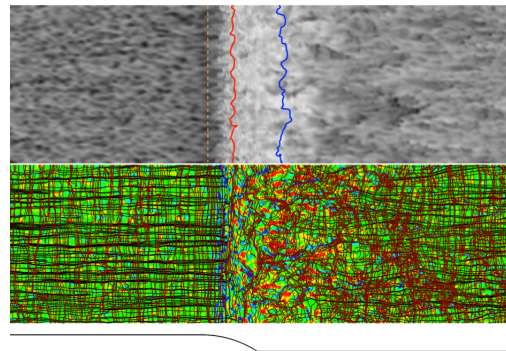


Figure 7. Surface flow pattern: Skin friction distribution together with separation and reattachment lines in red and blue, respectively, (top) and surface streamlines in black, vortex lines in dark red and contours of the first invariant of the no-slip tensor (bottom).

CONCLUDING REMARKS

We have used LES to simulate the development, separation, reattachment and gradual downstream recovery of the flow over the smoothly contoured ramp experiment of Song *et al.* (2000) and Song & Eaton (2004). Five subgrid models have been compared on a mesh of intermediate resolution containing 19.2 million cells, and the effect of mesh resolution has been examined by studying the behavior of the LDKM model on four different grids varying between 2.4 and 163.6 million cells.

For the time-averaged pressure coefficient, C_p , on the lower wall a comparison of the five different models on the intermediate grid shows that all models capture the favourable pressure gradient approaching the ramp, but that all models underestimate the pressure drop to some degree at the beginning of the ramp. Best agreement is obtained with the WALE and LDKM models, whereas the MM noticeably overpredicts the pressure around the reattachment line. The plots of C_p along the lower wall calculated using the LDKM model on all four grids are very similar, indicating that the grid resolution has minimal effect on C_p , as expected.

For the mean velocity, a comparison of the five models on the intermediate (19.6 Mcells) grid shows that the LDKM, WALE and ILES models all show virtually identical behavior, in good agreement with the experimental data, while the MM and OEEVM show departures from the experimental data in the separation region. As expected, the LDKM results show closer agreement with the experimental data as the grid is refined.

The results for the rms-velocity fluctuations show a similar trend to those of the mean velocity. On the intermediate grid the results of the WALE and LDKM models are very similar and agree well with the experimental results. The MM and OEEVM again show significant differences with the experimental results in the separation region, and the ILES model also performs poorly in this region. Once again, as the mesh is refined, the LDKM results show closer agreement with experiment.

In summary, we find that the LDKM and WALE simulation results are very similar and provide best overall agreement with experiment, and that for the axial velocity and rms-velocity fluctuations the LDKM results agree better with the experimental data as the grid is refined, while the C_p results appears virtually independent of the grid resolution.

REFERENCES

- Bardina J., Ferziger J.H. & Reynolds W.C.; 1980, "Improved Subgrid Scale Models for Large Eddy Simulations", AIAA Paper 80-1357.
- Bensow R. & Fureby C., 2008, "On the Justification and Extension of Mixed Models in LES", *J Turb.*, **8**, p N54.
- Chong M.S., Monty J.P., Chin C. & Marusic I.; 2012, "The Topology of Skin Friction and Surface Vorticity Fields in Wall-bounded Flows", *J. Turb.*, **13**, N6
- DeGraaff D.B. & Eaton J.K.; 1999, "Reynolds Number Scaling of the Turbulent Boundary Layer on a Flat Plate and on Swept and Unswept Bumps", Report TSD-118, Stanford University, Stanford, USA.
- Durbin P.A.; 1991, "Near-wall Turbulence Closure without Damping Functions", *Theo. Comp. Fluid Dyn.*, **3**, p 1.
- El-Askary W.A.; 2009, "Turbulent Boundary Layer Structure of Flow over a Smooth-Curved Ramp", *Comp. Fluids*, **38**, p 1718.
- Fureby C. & Grinstein F.F.; 2002, "Large Eddy Simulation of High-Reynolds-Number Free and Wall-Bounded Flows", *J. Comp. Phys.*, **181**, p 68.
- Germano M., Piomelli U., Moin P. & Cabot W.H.; 1991, "A Dynamic Subgrid-scale Eddy Viscosity Model", *Phys. Fluids*, **3**, p. 1760.
- Jasak, H.; 1996, "Error Analysis and Estimation for the Finite Volume Method with Application to Fluid Flows", Ph.D. thesis, Dept. Mech. Eng., Imperial College of Science, Technology and Medicine.
- Kim W.-W. & Menon S.; 1999, "A New Incompressible Solver for Large-Eddy Simulations", *Int. J. Num. Fluid Mech.*, **31**, p 983.
- Li Y., Chevillard L., Eyink G. & Meneveau C.; 2009, "Matrix Exponential-based Closures for the Turbulent Subgrid-Scale Stress Tensor", *Phys. Rev. E.*, **79**, 016305.
- Nicoud F., & Ducros F.; 1999, "Subgrid-Scale Stress Modeling Based on the Square of the Velocity Gradient Tensor", *Flow, Turb. & Comb.*, **62**, p 183.
- Margolin L.G. & Rider W.J.; 2002, "A Rationale for Implicit Turbulence Modelling", *Int. J. Num. Methods in Fluids*, **39**, p 821.
- Nikitin N.V., Nicoud F., Wasistho B., Squires K.D. & Spalart P.R.; 2000, "An Approach to Wall Modeling in Large-Eddy Simulations", *Phys. Fluids*, **12**, p 1629.
- Radhakrishnan S., Keating A. & Piomelli U.; 2006, "Large Eddy Simulations of High Reynolds-Number Flow over a Contoured Ramp", AIAA 2006-0899.
- Sagaut P.; 2001, "Large Eddy Simulation for Incompressible Flows", Springer Verlag, Heidelberg.
- Song S., DeGraaff D.B. & Eaton J.K.; 2000, "Experimental Study of a Separating, Reattaching and Redeveloping Flow over a Smoothly Contoured Ramp", *Int. J. Heat & Fluid Flow*, **21**, p 512.
- Song S. & Eaton J.K.; 2004, "Reynolds Number Effects on a Turbulent Boundary Layer with Separation, Reattachment, and Recovery", *Exp. in Fluids*, **36**, p 246.
- Spalart P.R. & Allmaras S.R.; 1994, "A One-Equation Turbulence Model for Aerodynamic Flows", *La Recherche Aerospatiale*, **1**, p 5.
- Yoshizawa A. & Horiuti K.; 1985, "A Statistically-Derived Subgrid Scale Kinetic Energy Model for Large Eddy Simulation of Turbulent Flows", *J. Phys. Soc. Japan*, **54**, p 2834.
- Wasistho B. & Squires K.D.; 2001, "Numerical Investigation of the Separated Flow over a Smoothly Contoured Ramp", *Turb. Shear Flow Phen.*, **2**, p 405
- Weller H.G., Tabor G., Jasak H. & Fureby C.; 1997, "A Tensorial Approach to CFD using Object Oriented Techniques", *Comp. in Physics*, **12**, p 629.

